PHYSICAL REVIEW E **88**, 051001(R) (2013)

Initial microfluidic dissolution regime of CO_2 bubbles in viscous oils

Martin Sauzade and Thomas Cubaud*

Department of Mechanical Engineering, Stony Brook University, Stony Brook, New York 11734, USA

(Received 11 July 2013; revised manuscript received 20 September 2013; published 8 November 2013)

We examine the initial dynamical behavior of dissolving microbubbles composed of carbon dioxide gas in highly viscous silicone oils over a range of flow rates and pressure conditions. Microfluidic periodic trains of CO_2 bubbles are used to probe the interrelation between bubble dissolution and high-viscosity multiphase flows in microgeometries. We investigate bubble morphology from low to large capillary numbers and calculate the effective mass diffusion flux across the interface by tracking and monitoring individual bubbles during shrinkage. The initial flux is characterized using a dissolution coefficient that reveals the influence of the oil molecular weight on the dissolution process. Our findings show the possibility to control and exploit the interplay between capillary and mass transfer phenomena with highly viscous fluids in small-scale systems.

DOI: 10.1103/PhysRevE.88.051001 PACS number(s): 47.55.dd, 47.61.Jd, 66.30.je, 68.03.−g

The dissolution of gas in liquid is a physicochemical phenomenon essential to life and the environment. Many natural and industrial flow processes depend on the rate of absorption and desorption of carbon dioxide gas in various fluids, including respiration [1], air-ocean interactions [2], effusive and explosive volcanic eruptions [3], advanced oil recovery [4], and polymer synthesis [5]. Better understanding the dynamics of dissolving bubbles in microgeometries is also important for the development of methods for the efficient capture of greenhouse gases in porouslike media.

Microfluidic platforms provide a simplified environment for examining multiphase transport properties at the pore level in the creeping flow conditions that are typically encountered in porous media [6]. Such devices are also useful for investigating the coupling between interfacial phenomena and flows [7–11]. Recent studies of segmented microflows have shown the possibility to enhance mixing and mass transfer coefficients due to the combination of large fluid interfacial area and liquid recirculation between bubbles [12–17]. While microfluidic studies have shed light on the dissolution dynamics of carbon dioxide gas in low-viscosity solvents [18–21], many technological fluids are highly viscous. In this case, bubbles are confined by a thick liquid film adjoining the solid walls and adopt a complex bullet shape depending on flow conditions [22]. Directly characterizing the combined effect of carbon dioxide absorption and diffusion processes in this situation would improve the modeling and practical use of high-viscosity carbonated microflows.

In this Rapid Communication, we scrutinize the initial dissolution of CO_2 bubbles within viscous silicone oils under various microflow conditions. Periodic and monodisperse trains of bubbles are generated at a focusing section and the bubble shape is monitored during forced convection mass transfer to study the relationship between dissolution dynamics and oil molecular weight.

The microfluidic liquid-gas contactor consists of an etched-through silicon piece that is anodically bonded between two borosilicate glass plates and placed on top of an inverted microscope equipped with a high-speed camera. Bubbles are generated at the junction of square channels of width $w = 250\ \mu$m [Fig. 1(a)]. Bone-dry gaseous CO_2 is injected from a pressurized tank to the central channel. A miniature regulator and a pressure sensor are used to finely control the gas injection pressure P_G and a flow meter measures the inlet gas volume flow rate Q_G along the gas-feeding line. Silicone oil is supplied at a flow rate of $Q_L/2$ in each side channel using high-pressure syringe pumps.

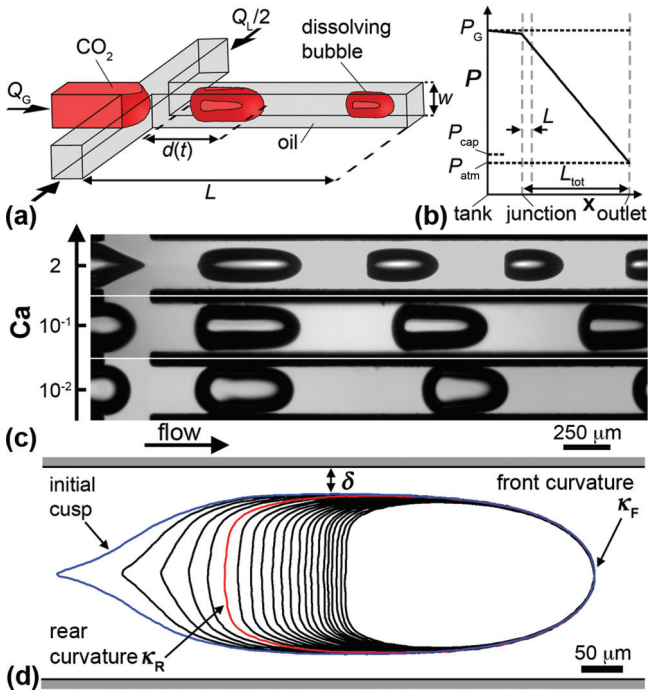

FIG. 1. (Color online) (a) Schematics of the microfluidic contactor. (b) Sketch of the typical pressure P along the central channel with $L \ll L_{tot}$ and $P \sim P_G$ near the fluid junction. (c) Micrographs of flow patterns with similar initial bubble size $d_0/w \approx 2.25$, flow rates in μL/min, and viscosity in cS: Ca ≈ 2 ($Q_L = 6$, $Q_G = 25$, and $\nu = 10^4$), Ca $\approx 10^{-1}$ ($Q_L = 380$, $Q_G = 341$, and $\nu = 10$), and Ca $\approx 10^{-2}$ ($Q_L = 800$, $Q_G = 670$, and $\nu = 1$). (d) Time series of bubble contour in the reference frame of the bubble front for Ca ≈ 2 ($\Delta t = 12$ ms).

*Author to whom correspondence should be addressed: thomas.cubaud@stonybrook.edu

We focus on early bubble dynamics near the fluid junction over a distance $L \sim 10w$. Since the total length of our microfluidic network $L_{tot} \sim 100w$ is large, the hydrodynamic resistance of pure gas flow is negligible in the inlet channel and the typical capillary pressure is small $P_{cap} \sim 4\gamma/w \approx 3 \times 10^{-3}$ atm, we neglect both frictional pressure drop and capillary pressure effects in our region of interest (ROI) and use P_G as a control parameter for the bubble pressure [Fig. 1(b)]. The test liquids are conventional polydimethylsiloxane oils with a kinematic viscosity ν ranging between 1 and 10^4 cS. Silicone oil is useful for investigating viscous flow phenomena since its viscosity depends on molecular weight M while other properties, such as density and surface tension, remain nearly constant. The wide range of viscosities probed, however, introduces large differences in flow rates and pressure for each fluid pair investigated. Indeed, assuming that the multiphase flow pressure drop $\Delta P = P_G - P_{atm}$ is essentially dominated by the large dynamic oil viscosity η according to $\Delta P = c\eta(Q_L+Q_G)L_{tot}/w^4$ with geometrical constant $c \approx 28.45$ [23,24], large flow rates are obtained with small pressure using low-viscosity oils and small flow rates are produced with large inlet pressure using high-viscosity oils. Nonetheless, our versatile fluid injection method and image acquisition system permit a systematic investigation of multiphase flows with both Q_L and Q_G varying between 10 and 10^3 μL/min and P_G between 1 and 5 atm. Accordingly, the typical bubble residence time $\tau \approx Lw^2/(Q_L + Q_G)$ in the ROI ranges between 1 and 10^3 ms.

In addition to introducing large differences in time scales, increasing liquid viscosity η significantly distorts the bubble shape. Examples of typical flow patterns are displayed in Fig. 1(c) from low to large capillary numbers $Ca = \eta U_B/\gamma$, where U_B is the average bubble velocity and γ is the surface tension. The low Ca regime is obtained for low-viscosity oils and typically consists of elongated bubbles having spherical end caps and lubricated by a thin liquid film near the walls. Such flows have been widely studied and are usually referred to as segmented or Taylor flows. Conversely, the high Ca regime is obtained for high-viscosity oils and corresponds to a situation where viscous effects dominate capillary effects. The lubricating film of thickness δ becomes large [25] and viscous confinement of capillary surfaces produces bubbles having a sharper nose. The recirculation region located behind the trailing meniscus and surrounding the flow centerline flattens the rear of the bubble and can even produce a reentrant cavity for very large Ca [26,27]. As a result, bubbles adopt a typical bullet shape and display a large front curvature κ_F and a small rear curvature κ_R.

Due to significant gas absorption, bubbles display a reduction in size during transport. To decorrelate dissolution from convection, we adopt a Langrangian approach [28] and track individual bubbles to digitally extract their contours as a function of time and location using custom-made IMAGEJ scripts and MATLAB codes. Contours are then superposed onto a composite image for inspection. For low Ca flows, elongated bubbles suffer a longitudinal shrinking while front and rear curvatures are set with the channel geometry $\kappa_F \sim \kappa_R \sim 2/w$. For low-viscosity oils at high flow rates, with associated Reynolds number $Re \sim 200$, we observe the generation of surface waves along the bubble in the few instants following breakup. Such waves, however, are quickly dampened as bubbles are convected downstream in the fully developed flow. During high Ca flows, the bubble shape is characterized by the presence of a sharp cusp following breakup from the gas-feeding channel [29]. This cusp quickly recedes in the bulk and bubbles assume a bulletlike shape with significant differences between front and rear curvatures $\kappa_F \gg \kappa_R$ depending on Ca. To visualize bubble deformation, it is convenient to align time-series contours with the bubble front [Fig. 1(d)]. In this case, the very viscous fluid acts as a sheath material and strongly confines bubbles to Stokes flow in a square duct.

To measure the mass diffusion flux during dissolution, it is important to determine the instantaneous bubble volume $\Omega(x,t)$ and interfacial area $A(x,t)$. To this end, we use our two-dimensional contours to reconstruct three-dimensional bubble shapes. We assume the profile in the third dimension conforms to the contour plots of the velocity field of a single laminar flow in a square channel. Longitudinally slicing bubbles in pixel-wide "disks" of diameter D_c allows us to estimate their area A_c using the roundness parameter $r = 4A_c/(\pi D_c^2)$ of the associated contour plot of the velocity field circumscribing the bubbles [Fig. 2(a)]. The bubble volume $\Omega(x,t)$ is then simply calculated by summing individual areas A_c over the length of the bubble. Similarly, the bubble interfacial area $A(x,t)$ is computed by adding the perimeters of the disks associated with purely viscous flows.

We validate our bubble volume calculation method by comparing the inlet gas flow rate Q_G with its *in situ* counterpart measurement Ω_0/T, where Ω_0 is the initial volume of the

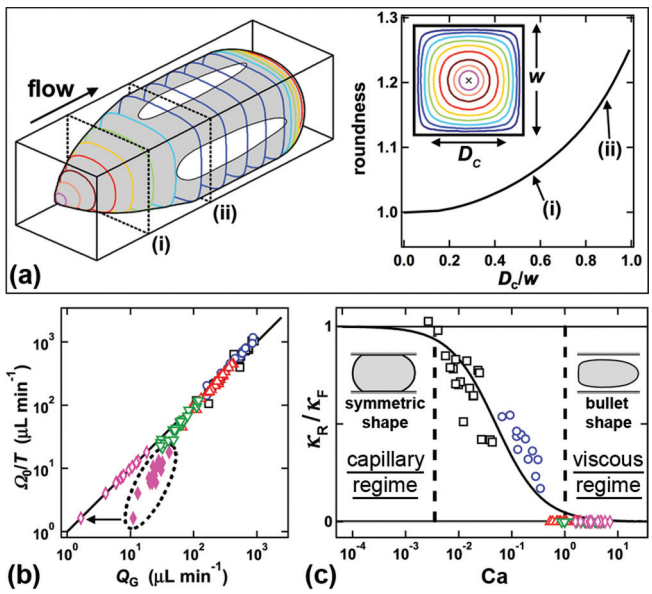

FIG. 2. (Color online) (a) Schematic of volume reconstruction method using the roundness r of velocity contour plots of a single viscous flow in a square duct to calculate the geometrical parameters of each bubble slice. (b) Comparison between local gas flow rate Ω_0/T and the inlet gas flow rate Q_G. Small flow rates Q_G associated with highly viscous oil are calibrated using the local flow rate (arrow). The solid line denotes $\Omega_0/T = Q_G$, with oil viscosity $\nu = 1$ (□), 10 (○), 10^2 (△), 10^3 (▽), and 10^4 cS (◇). (c) Ratio between the rear cap curvature and the front cap curvature vs capillary number. The solid line denotes $\kappa_R/\kappa_F = (1 + Ca/Ca_c)^{-1}$, with $Ca_c = 5 \times 10^{-2}$.

bubble after breakup and T is the period of the bubble formation [Fig. 2(b)]. The calculated volume of deformed viscous bubbles (*e.g.*, $\nu = 10^2$ and 10^3 cS) is in agreement with the input parameter. We note, however, a significant discrepancy between the two measurements for the highly viscous situation ($\nu = 10^4$ cS). The very small gas flow rate produced in this case falls into the lower range of the flow meter operating conditions (for Q_G below $\sim$30 μL/min), which systematically overestimates Q_G. In this case, we use the local flow rate measurement Ω_0/T as a reference to compute the actual gas flow rate Q_G.

As elongated droplets are often described with ellipses [30,31], we fit the front and rear caps of individual bubbles with ellipses having a semimajor axis a and semiminor axis b to calculate front and rear curvatures using $\kappa = a/b^2$. We find that the ratio of the rear to the front curvature κ_R/κ_F is an original and useful parameter to describe bubble shape in confined microgeometries and allows for examining the crossover between purely capillary (Ca $< 10^{-2}$) and viscous regimes (Ca $> 5 \times 10^{-1}$). A simple estimate for the regime transition is obtained when $\kappa_R/\kappa_F = 1/2$ and corresponds to the critical capillary number Ca$_c \approx 5 \times 10^{-2}$ [Fig. 2(c)].

For every flow condition, the instantaneous bubble length d, interfacial area A, and volume Ω are computed by digitally processing high-speed movies (Fig. 3). To solely focus on gas dissolution effects, the time is set to zero when the bubble rear is at a distance w from the junction. This method allows for alleviating complex shape effects due to breakup with the presence of quickly damped surface waves for low Ca and rapidly receding rear cusps for large Ca. This approach results in no more than 15% truncation of the total bubble residence time in the ROI. Following this operation, two general trends are apparent. At low Ca, bubble shape parameters decrease steadily, while at high Ca, parameters first exhibit a steady decrease before slowly stabilizing for longer times.

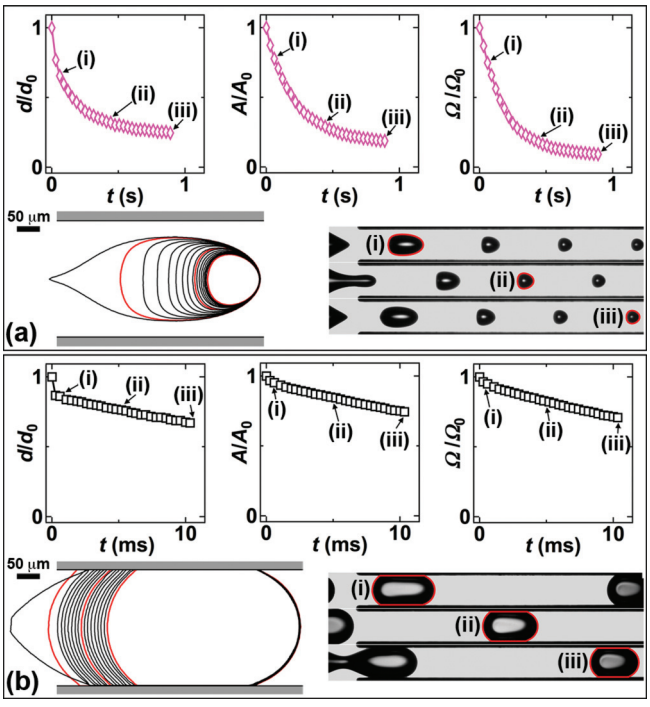

FIG. 3. (Color online) Temporal evolution of the normalized bubble size d/d_0, interfacial area A/A_0, and volume Ω/Ω_0 in the ROI: (a) viscous regime, Ca = 1.1, $\nu = 10^4$ cS, and $P_G = 2.7$ atm and (b) capillary regime, Ca $= 9 \times 10^{-3}$, $\nu = 1$ cS, and $P_G = 1.03$ atm.

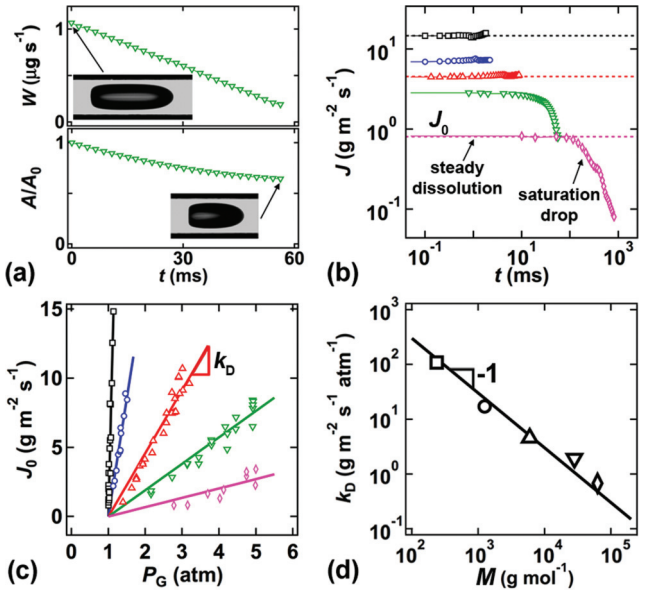

FIG. 4. (Color online) Diffusive mass flux of CO_2 bubbles in silicone oils. (a) Example of evolution of diffusive mass flow rate W and interfacial area A for $\nu = 10^3$ cS. (b) Examples of mass diffusion flux J with constant initial flux J_0 for various oils, $\nu = 1$ (□), 10 (○), 10^2 (△), 10^3 (▽), and 10^4 cS (◇). (c) Early flux J_0 versus pressure P_G for all fluid pairs. The solid lines denote $J_0 = k_D(P_G - P_{atm})$. (d) Dissolution coefficient k_D as a function of oil molecular weight M. The solid line denotes $k_D = 3 \times 10^4/M$.

The temporal evolution of bubble shape at a given pressure P_G allows us to measure the net mass flux according to $J = \rho_{CO_2}[d(\Omega_0-\Omega)/dt]/A$, where $\rho_{CO_2} = \rho_0 P_G/P_{atm}$ and ρ_0 is the standard density of CO_2. Mass transfer operations are often described using a liquid mass transfer coefficient k_L to relate mass flux and variation of solute concentration $J = k_L \Delta C$. Here measurements of J at the bubble level are useful to examine the influence of flow and fluid properties on gas absorption in microgeometries. In the early dissolution regime, data show a linear temporal evolution of both the dissolution rate $W = \rho_{CO_2} d(\Omega_0 - \Omega)/dt$ and the interfacial area A [Fig. 4(a)], which results in a steady mass flux J_0 before a sharp decrease for long residence times [Fig. 4(b)]. The ensuing decline in J is attributed to a solute concentration in the bulk reaching near equilibrium with the interfacial concentration $\Delta C \sim 0$ and is referred to as saturation drop. This phenomenon is not observed for low-viscosity flows due to their short bubble residence times in the ROI. For each fluid pair, we calculate the early steady diffusive flux J_0 and find a linear relationship with pressure according to $J_0 = k_D \Delta P$, where $\Delta P = P_G - P_{atm}$ and k_D is the dissolution coefficient [Fig. 4(c)]. This behavior can be understood considering the mechanisms involved in the gaseous dissolution. As the bulk oil concentration C_{oil} is initially negligible due to the low partial pressure of CO_2 in the air, it follows that in the liquid interfacial region $\Delta C \approx C_i$, where the solubility concentration C_i depends on pressure according to $C_i = P_G/k_H$, with k_H

being the Henry constant. Therefore, the early mass flux J_0 is expected to scale with P_G with a dissolution coefficient $k_D \approx k_L/k_H$. Our experimental findings show that when the solvent is initially exposed to air, J_0 scales with the gage injection pressure ΔP. This fact suggests an exchange of species with absorption of carbon dioxide and desorption of previously dissolved nitrogen and oxygen molecules into the bubble. As a result, the solvent effectively behaves as initially saturated with CO_2 at atmospheric pressure. Overall, the coefficient k_D is a reliable parameter for characterizing the dissolution rate of given fluid pairs and it combines the two fundamentals of gas absorption, namely, saturation through k_H and the dynamics at which the system approaches equilibrium with k_L [32].

Liquid mass transfer rates k_L through a moving interface are typically determined using a penetration model with $k_L \sim (D/\tau_c)^{1/2}$, where D is the diffusion coefficient and τ_c the liquid contact time, i.e., the convective time scale [33]. By contrast, in the case of a stagnant film, only molecular flux is considered and Fick's first law yields $k_L \sim D/\varepsilon$, where ε is the concentration thickness. A cylindrical bubble in a square channel combines equivalents of both moving and stagnant liquid-gas mass transfer surfaces with (a) the sides in contact with the liquid film near the walls and (b) the end caps. Previous work in the capillary regime showed that dissolution primarily occurs through bubble end caps [19]. This situation is analogous to the stagnant film model since gas is transferred into reservoirs of liquid traveling along with bubbles. Recirculation motion in such liquid plugs tends to homogenize bulk concentration C_{oil} and confines solute concentration variations to a thin liquid boundary layer of thickness ε at the transfer surface.

For the CO_2–silicone oil fluid pairs, the dissolution dynamics strongly depends on the oil molecular structure. We express the oil viscosity η as a function of molecular weight M and k_D is found to steadily decrease with M according to $k_D \approx aM^{-1}$, with the prefactor $a = 3 \times 10^4$ g^2/(mol m^2 s atm) [Fig. 4(d)]. As the concentration thickness is expected to be proportional to the polymer hydrodynamic radius $\varepsilon \sim M^{1/2}$, our finding for k_D suggests that $D/k_H \sim M^{-1/2}$. According to the theory of the diffusion of polymer, diffusivity depends on polymer concentration and molecular interactions and ranges between $D \sim M^{-1/2}$ for a dilute solution of polymer in a low-viscosity solvent and $D \sim M^{-2}$ for self-diffusion in an undiluted polymer [33]. In particular, if hydrodynamic interactions between individual polymers are neglected, theory predicts $D \sim M^{-1}$. Assuming such scaling for D yields a dependence for the Henry constant such as $k_H \sim M^{-1/2}$ and implies that carbon dioxide solubility $C_i \sim k_H^{-1}$ weakly increases with the polymer molecular weight M. These arguments illustrate the complexity in relating dissolution dynamics to fluid properties since models used for k_L, ε, and D strongly affect results for solubility. From a practical standpoint, the determination of k_D for a given liquid-gas pair provides a more reliable and direct estimate of gas impregnation dynamics.

In this study, we analyze the morphology of dissolving carbon dioxide bubbles in oils from low to large capillary numbers and we extract the initial steady mass transfer flux during gas absorption. We show that the dissolution mass transfer coefficient k_D is a practical parameter to quantify diffusive multiphase flow phenomena in microgeometries. In particular, its systematic characterization is useful for comparing data with forced-convection mass transfer processes and fluid properties models. Further developments should consider the influence of gas exchange on partial pressure balance inside bubbles, as well as polymer swelling [34] and potential modification of diffusion and solubility coefficients during absorption [35]. Theoretical and numerical investigations would provide insights into the factors affecting microfluidic dissolution processes. This study is promising for the development of high-viscosity fluid microflow contactors and for better characterizing gas dissolution processes in complex fluids using microfluidic passages.

This material is based upon work supported by the National Science Foundation under Grant No. CBET-1150389.

[1] J. B. West, *Respiratory Physiology: The Essentials* (Lippincott Williams & Wilkins, Philadelphia, 2012).
[2] B. Jahne and H. Haussecker, Annu. Rev. Fluid Mech. **30**, 443 (1998).
[3] H. M. Gonnermann and M. Manga, Annu. Rev. Fluid Mech. **39**, 321 (2007).
[4] H. Fadaei, B. Scarff, and D. Sinton, Energ. Fuel. **25**, 4829 (2011).
[5] D. L. Tomasko, H. B. Li, D. H. Liu, X. M. Han, M. J. Wingert, L. J. Lee, and K. W. Koelling, Ind. Eng. Chem. Res. **42**, 6431 (2003).
[6] J. Bear, *Dynamics of Fluids in Porous Media* (Dover, New York, 1988).
[7] T. M. Squires and S. R. Quake, Rev. Mod. Phys. **77**, 977 (2005).
[8] P. Garstecki, H. A. Stone, and G. M. Whitesides, Phys. Rev. Lett. **94**, 164501 (2005).
[9] B. Dollet, W. van Hoeve, J.-P. Raven, P. Marmottant, and M. Versluis, Phys. Rev. Lett. **100**, 034504 (2008).
[10] P. Poesio, G. P. Beretta, and T. Thorsen, Phys. Rev. Lett. **103**, 064501 (2009).
[11] M. Abkarian, A. B. Subramaniam, S.-H. Kim, R. J. Larsen, S.-M. Yang, and H. A. Stone, Phys. Rev. Lett. **99**, 188301 (2007).
[12] A. Gunther, M. Jhunjhunwala, M. Thalmann, M. A. Schmidt, and K. F. Jensen, Langmuir **21**, 1547 (2005).
[13] M. T. Kreutzer, F. Kapteijn, J. A. Moulijn, and J. J. Heiszwolf, Chem. Eng. Sci. **60**, 5895 (2005).
[14] R. Pohorecki, Chem. Eng. Sci. **62**, 6495 (2007).
[15] T. Cubaud, M. Sauzade, and R. Sun, Biomicrofluidics **6**, 22002 (2012).
[16] J. Tan, Y. C. Lu, J. H. Xu, and G. S. Luo, Chem. Eng. J. **181**, 229 (2012).
[17] P. Sobieszuk, J. Aubin, and R. Pohorecki, Chem. Eng. Technol. **35**, 1346 (2012).
[18] J. I. Park, Z. Nie, A. Kumachev, and E. Kumacheva, Soft Matter **6**, 630 (2010).
[19] R. Sun and T. Cubaud, Lab Chip **11**, 2924 (2011).
[20] M. Abolhasani, M. Singh, E. Kumacheva, and A. Gunther, Lab Chip **12**, 1611 (2012).

[21] S. G. Lefortier, P. J. Hamersma, A. Bardow, and M. T. Kreutzer, Lab Chip **12**, 3387 (2012).
[22] V. S. Ajaev and G. M. Homsy, Annu. Rev. Fluid Mech. **38**, 277 (2006).
[23] F. M. White, *Viscous Fluid Flow* (McGraw-Hill, New York, 1991).
[24] T. Cubaud and C.-M. Ho, Phys. Fluids **16**, 4575 (2004).
[25] W. B. Kolb and R. L. Cerro, Chem. Eng. Sci. **46**, 2181 (1991).
[26] T. Taha and Z. F. Cui, Chem. Eng. Sci. **61**, 665 (2006).
[27] M. D. Giavedoni and F. A. Saita, Phys Fluids **11**, 786 (1999).
[28] G. K. Batchelor, *An Introduction to Fluid Mechanics* (Cambridge University Press, New York, 1967).
[29] K. Pancholi, E. Stride, and M. Edirisinghe, Langmuir **24**, 4388 (2008).
[30] H. A. Stone and L. G. Leal, J. Fluid Mech. **211**, 123 (1990).
[31] J. T. Cabral and S. D. Hudson, Lab Chip **6**, 427 (2006).
[32] W. K. Lewis and W. G. Whitman, Ind. Eng. Chem. **16**, 1215 (1924).
[33] R. B. Bird, W. E. Stewart, and E. N. Lightfoot, *Transport Phenomena* (Wiley, New York, 2002).
[34] J. R. Royer, J. M. DeSimone, and S. A. Khan, Macromolecules **32**, 8965 (1999).
[35] F. W. Wu, L. Li, Z. H. Xu, S. J. Tan, and Z. B. Zhang, Chem. Eng. J. **117**, 51 (2006).